Deciphering Structure and Charge Carrier Behavior in Reduced-Dimensional Perovskites

Kun Sun, Renjun Guo,* Shangpu Liu, Dengyang Guo, Xiongzhuo Jiang, Linus F. Huber, Yuxin Liang, Manuel A. Reus, Zerui Li, Tianfu Guan, Jungui Zhou, Matthias Schwartzkopf, Samuel D. Stranks, Felix Deschler, and Peter Müller-Buschbaum*

Reduced-dimensional perovskites (RDPs) have advanced perovskite optoelectronic devices due to their tunable energy landscape, structure, and orientation. However, the origin of structural and photophysical property changes when moving from low-dimensional to high-dimensional RDPs remains to be understood. This study systematically reveals structural and photophysical properties of slot-die-coated Dion-Jacobson (DJ) and Ruddlesden-Popper (RP) RDPs with different dimensionalities. RP RDPs with lower dimensionality ($n = 2$) exhibit a dominant $n = 2$ phase, preferential out-of-plane orientation, and longer charge carrier lifetime compared with DJ RDPs. In addition, the formation kinetics of RDPs with higher dimensionality ($n = 4$) are unraveled by in situ X-ray scattering, showing the favorable formation of the lower-n phase in RP RDPs. The formation of these lower-n phases is thermodynamically and stoichiometrically favored, while these phases are likely in the form of an "intermediate phase" which bridges the 3D-like and lower-n phases in DJ RDPs. DJ RDPs with higher dimensionality demonstrate comparable phase purity, preferential orientation, spatially vertical phase homogeneity, and longer charge carrier lifetime. As such, DJ-based perovskite solar cells (PSCs) ($n = 4$) demonstrate better photostability under operational conditions than RP-based PSCs. Thus, the work paves the way for the utilization of RDPs to upscale PSCs.

1. Introduction

Reduced-dimensional (2D and quasi-2D) perovskites (RDPs) with intriguing physical and structural properties,[1,2] have emerged as promising candidates in photovoltaics,[3–6] light-emitting devices,[7] and next-generation optoelectronics devices.[8] RDPs are perovskite quantum wells (QWs) separated by bulky organic cations, in which the width (n) of the RDPs is determined by the thickness of the $[PbI_6]4^-$ octahedra. Two typical RDPs, i.e., Dion-Jacobson (DJ) and Ruddlesden-Popper (RP) perovskites, have the chemical formulas of $LA_{n-1}Pb_nI_{3n+1}$ and $L''_2A_{n-1}Pb_nI_{3n+1}$, where L, L,'' and A refer to the divalent, monovalent organic spacer cations, and monovalent cations, respectively. In general, a number of factors, e.g., the stoichiometry of the perovskite precursor,[9] ligand type and size,[10,11] additives,[12,13] fabrication methods,[14,15] jointly affect the phase

K. Sun, X. Jiang, L. F. Huber, Y. Liang, M. A. Reus, Z. Li, T. Guan,
P. Müller-Buschbaum
TUM School of Natural Sciences
Department of Physics
Chair for Functional Materials
Technical University of Munich
James-Franck-Str. 1, 85748 Garching, Germany
E-mail: muellerb@ph.tum.de
R. Guo
Laboratory of Zhongyuan Light
School of Physics
Zhengzhou University
100 Kexue Avenue, Zhengzhou 450001, China
E-mail: renjun@zzu.edu.cn

R. Guo
Institute of Microstructure Technology
Karlsruhe Institute of Technology
Hermann-von-Helmholtz-Platz 1
76344 Eggenstein-Leopoldshafen, Germany
S. Liu, F. Deschler
Physikalisch-Chemisches Institut
Universität Heidelberg
Im Neuenheimer Feld 229, 69120 Heidelberg, Germany
D. Guo, S. D. Stranks
Chemical Engineering and Biotechnology
University of Cambridge
Cambridge CB3 0AS, UK
J. Zhou, M. Schwartzkopf
Deutsches Elektronen-Synchrotron DESY
Notkestraße 85, 22607 Hamburg, Germany

ADVANCED
SCIENCE NEWS

www.advancedsciencenews.com

ADVANCED
FUNCTIONAL
MATERIALS

www.afm-journal.de

distributions of RDPs. A mixture of multiple dimensionalities of RDPs with random crystal orientation is expected to build up during the film formation process.[4,16,17] Such phase impurities may introduce an inhomogeneous energy landscape and impede charge transport.[18–20] Therefore, it is imperative to investigate the phase distribution and crystal orientation of RDPs, which necessitates studying their growth kinetics, as these characteristics are determined during film growth. However, despite some pioneering work on the growth kinetics of RP RDPs,[21,22] a comprehensive study combining the growth mechanisms of both, RP and DJ RDPs in a large-scale deposition is still missing.

In addition to the growth kinetics, the organic cations heavily influence the structural distortion and interlayer screening, resulting in their different photophysical properties, e.g., binding energy and charge carrier mobility.[23] In particular, the coupling of inorganic anions and organic spacers in RDPs facilitates the electron-phonon reaction, resulting in high nonradiative charge recombination and shorter charge carrier lifetimes.[24] Therefore, understanding the function of organic ligands on the phase purity, growth mechanism, and charge carrier dynamics is beneficial for directing the usage of RDPs in 2D/3D heterojunction and quasi-2D solar cell applications.

To fill this gap and enable the advancement of large-scale deposition of RDPs, we focus on the slot-die coated RP and DJ RDPs with varying dimensionalities (n = 2 or 4), i.e., $(PEA)_2MA_{n-1}Pb_nI_{3n+1}$ (PEA: phenethylammonium) and $(PDMA)MA_{n-1}Pb_nI_{3n+1}$ (PDMA: 1,4-phenylenedimethanammonium), owing to their chemical similarities and extensive applications in the field.[25,26] Using grazing incidence wide-angle X-ray scattering (GIWAXS), we determine the phase distribution and orientations of respective RDPs, highlighting the different phase composition in RDPs with higher dimensionality. We further monitor the film growth of RDPs (n = 4) during slot-die coating with in situ scattering techniques, showing the stoichiometry-determined phase formation. With the help of transient absorption (TA) spectroscopy, we unravel the phase purity, charge carrier behavior, and energy transfer in respective RDPs. We further test the intrinsic stability of perovskite solar cells (PSCs) based on RP and DJ (n = 4) RDPs under the protocol of ISOS-L-1I with operando GIWAXS, showcasing the overall better stability of DJ-based PSCs. Our work leverages the understanding of structural-photophysical properties in RP and DJ materials with different dimensionalities, thus advancing the utilization of 2D perovskites as passivation layers and promoting the fabrication of efficient quasi-2D PSCs.

2. Result

Multiple n-value phases of RDPs are naturally formed during the crystallization, resulting in an inhomogeneous energy landscape and inefficient energy transfer.[3,27] Identifying the phase distributions and their orientations enables a deeper understanding of the charge carrier dynamics. Therefore, we perform GIWAXS measurements at different incident angles (α_i, 0.2°–0.6°) to investigate the vertically spatial phase distribution (**Figure 1**; Figure S1, Supporting information). We find that the lower-n phases (normally below 1 Å^{-1}) and 3D-like phase (≈1 Å^{-1}) of RP and

DJ RDPs (n = 2) present with the increase α_i, indicating that these phases are distributed homogenously throughout the film. The reshaped 2D GIWAXS data at α_i = 0.6° (Figure S2, Supporting information) illustrate that the RP RDPs exhibit a preferential orientation (Bragg peaks) along the out-of-plane direction. In contrast, DJ RDPs appear to be predominantly isotropic with a partially vertical orientation.

In terms of high-dimensional RDPs, with an increased scattering depth, the peak of lower-n phases in RP RDPs (n = 4) becomes more prominent (Figure 1E; Figure S3A–C, Supporting information), corroborating that lower-n phases are prone to be present in the interior of the RP film and their phase heterogeneity along the vertical direction. In contrast, the signals of lower-n phases in DJ RDPs (n = 4) are indiscernible (Figure 1F; Figure S3D-F, Supporting information), meaning an insufficient presence of lower-n phases in DJ RDPs and their spatially vertical phase homogeneity. This structure variance in RP and DJ RDPs illustrates that DJ RDPs with higher dimensionality are prone to form phase-pure perovskite. On the other hand, the signals at lower α_i in both RP and DJ RDPs (n = 4) are predominantly 3D-like phases, manifesting that the 3D-like phase tends to stack at the air-substrate interface. In addition, the PL spectra (Figure S4, Supporting information) excited from front and back (glass side) show that the intensities at peak ≈570 nm (back) are higher, implying that the lower-n phases are mainly located at the bottom of the films, in agreement with GIWAXS data. In light of the favorable formation of a 3D-like phase and phase distribution along the vertical direction,[21] we can deduce that the nucleation of RDPs (n = 4) starts at the air-precursor interface. Knowing where the nucleation and crystallization take place and locating these n-value phases enable suppressing the lower-n phase and realizing a homogenous energy landscape. Furthermore, with the increased dimensionality, the orientation of perovskite crystals becomes less pronounced, shifting from a predominantly vertical or partially vertical alignment to a more isotropic orientation. Notably, DJ RDPs show distinct orientations at χ = 0°,45° and 80° (Figure S5, Supporting information) compared to RP RDPs (oriented mainly at χ = 0°). In addition, to retrieve the crystal orientation distribution, we calculate the material quantity by correcting the intensity with a factor of $\sin\chi$ (Figure S5, Supporting information).[28] We notice an increase in oriented crystal contribution in DJ RDPs (43%) in comparison to RP RDPs (23%), suggesting their preferential orientation and potentially higher efficiency for charge transport.

Taken together, the schematic illustration of the respective RDPs is depicted in Figure 1. In short, the 3D-like phase and lower-n phases of RP and DJ (n = 2) are homogenously distributed throughout the film, where the RP and DJ crystals are vertically oriented and partially vertically oriented, respectively. With increasing dimensionality, the texture becomes weaker in both RP and DJ RDPs. Moreover, we notice multiple n-values phases coexist in RP film (n = 4), with stacking of substrate/lower-n phase/3D-like phase, whereas the lower-n phase is invisible in DJ RDPs. These results indicate that RP RDPs with lower dimensionality have a preferential orientation along the out-of-plane direction compared to DJ, which facilitates charge transport. In contrast, DJ RDPs (n = 4) demonstrate an improved phase purity and a more pronounced orientation distribution (43%) compared to RP RDPs (23%).
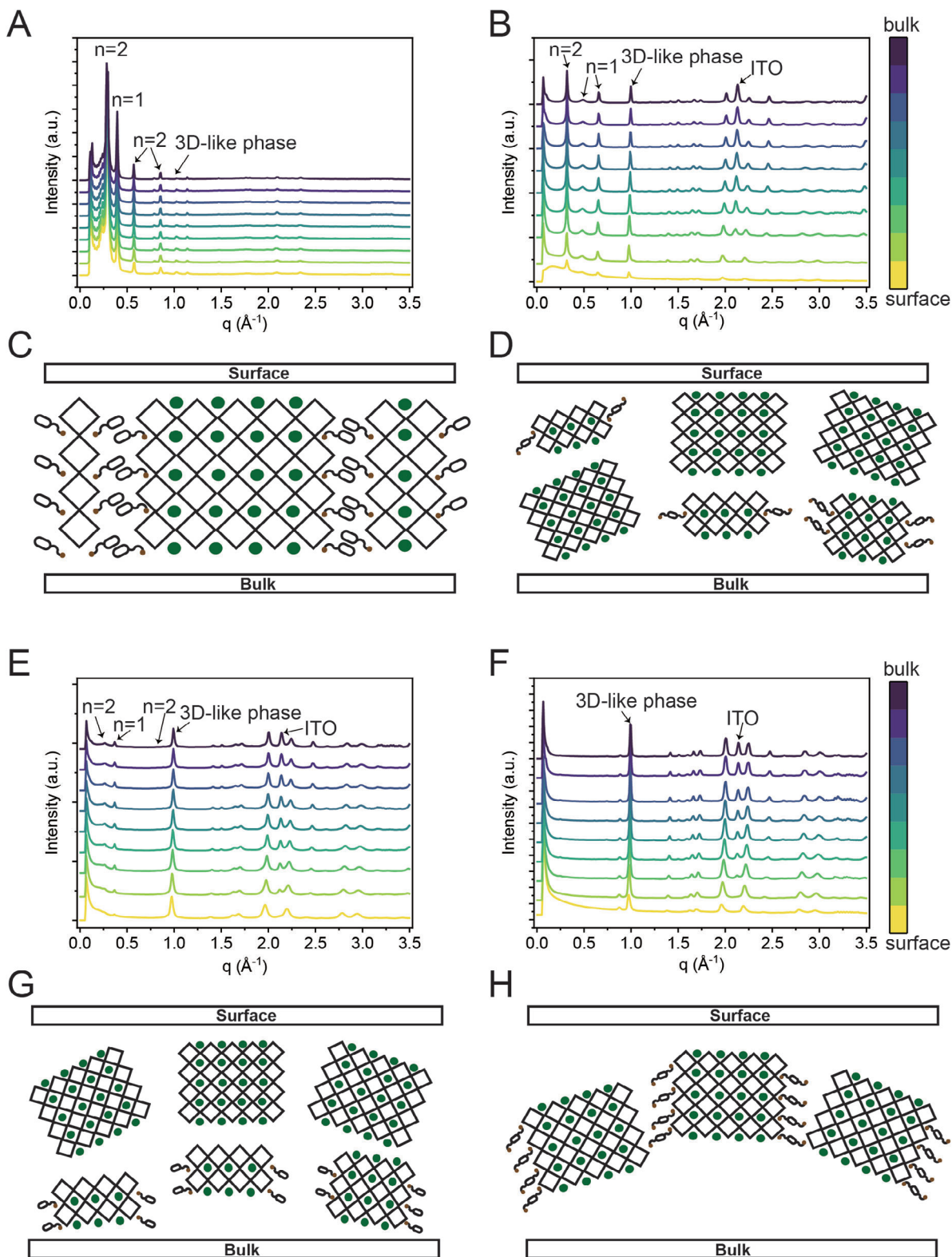
**ADVANCED
SCIENCE NEWS**

www.advancedsciencenews.com

**ADVANCED
FUNCTIONAL
MATERIALS**

www.afm-journal.de

Figure 1. Phase distributions and schematic illustration of RDPs film. Angular-dependent pseudo-XRD was extracted from 2D GIWAXS data with varying incident angles, in which the different phases of RDPs and the ITO peak are indicated. A) RP RDPs ($n = 2$) and B) DJ RDPs ($n = 2$). Schematic illustration of the structures of RDPs ($n = 2$). C) RP RDPs, where the crystals are vertically oriented, and D) DJ RDPs, in which the 3D-like phase and lower-n phase are partially vertically oriented. Angular-dependent pseudo-XRD of E) RP RDPs ($n = 4$), showing the increased quantity of lower-n phases with increasing depth and F) DJ RDPs ($n = 4$). Schematic illustration of the structures of RDPs ($n = 4$). (G) RP RDPs, showing that the majorities are randomly oriented and the lower-n phase is distributed in the interior of the film, and H) DJ RDPs, exhibiting their phase purity and orientations at $\chi = 0°$ and $45°$.

ADVANCED
SCIENCE NEWS

www.advancedsciencenews.com

ADVANCED
FUNCTIONAL
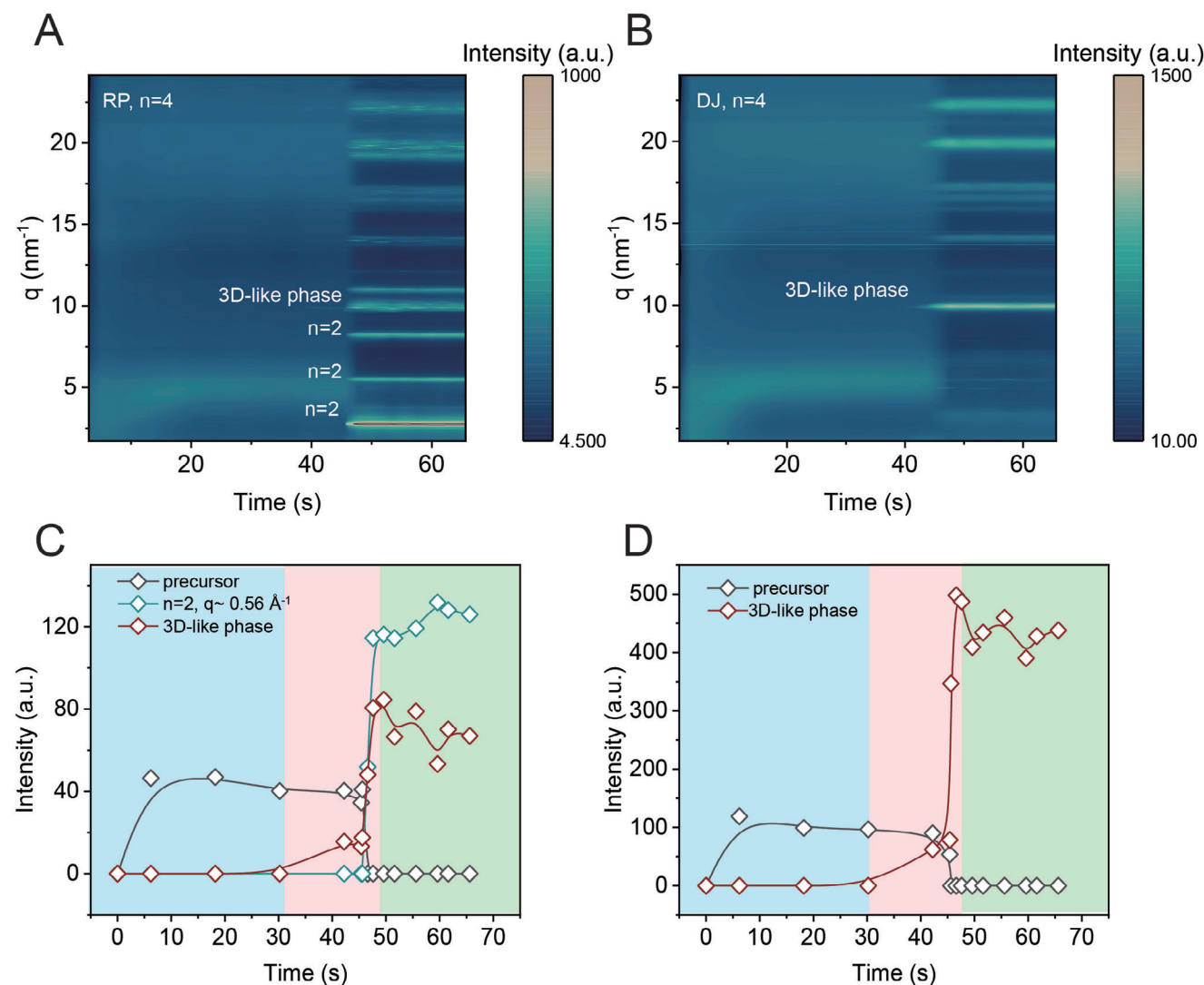**MATERIALS**

www.afm-journal.de

Figure 2. Growth kinetics of RP and DJ RDPs ($n = 4$) on ITO substrates. 2D color plots of radially integrated line profiles of in situ GIWAXS data, where the prominent peaks are indicated. A) RP RDPs film and B) DJ RDPs film. The normalized integrated intensity of the selected Bragg peaks as a function of time for C) RP and D) DJ RDPs. This shows the conversion of precursor (broad peak at $q \approx 0.5 \text{ Å}^{-1}$) to the final quasi-2D perovskite film, where the Bragg peaks of $q \approx 0.56$ and $q \approx 1.0 \text{ Å}^{-1}$ represent the lower-n phase (040) and 3D-like phase of RDPs. The color background indicates the different regimes of RDPs growth.

To disclose the structural and orientational disparities in RDPs ($n = 4$), we perform synchrotron-based in situ GIWAXS (**Figure 2A,B**) to monitor the growth kinetics during film growth. We observe two broad isotropic rings at ≈ 0.5 and $\approx 1.9 \text{ Å}^{-1}$ in both RP and DJ RDPs ($n = 4$, Figures S6A and S7A, Supporting information) for the first 40 s, representing the colloidal precursor sol-gels. Selected 2D reshaped GIWAXS data (Figures S6 and S7, Supporting information) of RP and DJ RDPs show the representative features at different timescales during film growth. After 40 s, the broad rings start to diminish, and the 3D-like phase appears. We do not observe any intermediate phase (e.g., 2MAI • PbI$_2$ • 2DMF) during film growth, likely due to the higher substrate temperature, which suppresses the formation of an intermediate phase.[29] To quantify the conversion of the precursor and the formation of RDPs, the peak intensities

of the precursor, 3D-like phase, and $n = 2$ phase ($q \approx 0.56 \text{ Å}^{-1}$) are extracted and plotted (Figure 2C,D). The conversion rate of the precursor peak mirrors the formation of the 3D-like phase, indicating a direct transition from precursor to RDPs in both studied cases. Interestingly, the emergence of the 3D-like phase (at ≈ 40.2 s) precedes the formation of the $n = 2$ phase in RP RDPs (≈ 45.6 s). This difference is related to the stoichiometry and formation energy, i.e., the formation of the 3D-like phase is more thermodynamically favored compared with lower-n phases.[30]

In addition, we find that many lower-n phases coexist in RP, while these signals are indiscernible in DJ RDPs, in accordance with angular-dependent GIWAXS data. Such phenomena are correlated with three factors: a) The stoichiometries of RDPs ($n = 4$), particularly the concentration of long ligands in relation

2411153 (4 of 11)

to MA$^+$, determine the formation of lower-n phase such that the formation of lower-n phases in RP RDPs is more favorable compared to DJ RDPs. To test this, we monitor the growth of RP RDPs ($n = 2$) under the same conditions with in situ GIWAXS (Figure S8, Supporting information). It is found that lower-n phases ($q \approx 0.28$ Å^{-1}) are formed prior to the formation of a 3D-like phase, which is ascribed to the higher concentration of long ligands than that of MA$^+$; b) We infer that there might be an insufficient presence of lower-n phase or some "intermediate phases" bridging the 3D-like phase and lower-n phases in DJ RDPs, likely not yielding the signal of lower-n phase in GIWAXS;[22] c) The lower formation energies of the lower-n phases in RP RDPs facilitate their formation in comparison to their DJ analogs.[31–33]

The schematic illustrations (Figure S10, Supporting information) summarize the formation kinetics of RP and DJ RDPs ($n = 4$), showing the individual events that occur during the film growth. In terms of RP formation, first, the solvent-perovskite complex provides the scaffold that can facilitate the nucleation and the construction of the QWs,[34] followed by the formation of a weakly-textured 3D-like phase at the air-film interface. Continuous nucleation leads to the formation of lower-n phases that consume a large portion of long ligands, which in turn leave the short-chain precursors and promote the further growth and re-orientation of the 3D-like phase. Considering the different formation rates of lower-n and 3D-like phases in RP and the location of these lower-n phases (i.e., the interior of the film), further efforts should be devoted to employing buried interface engineering, e.g., using ligands that can anchor lower-n phases to achieve controllable the growth and the orientation of these phases. In contrast, DJ RDPs undergo a direct transformation from precursor to 3D-like phase and "intermediate phase." It is also worth mentioning that the film formation processes of slot-die coating and one-step spin-coating for RDPs are quite similar, as they both involve three stages: sol-gel, 3D-like perovskite, and 2D perovskite formation.[21]

To further determine the phase purity and the charge carrier behavior of RDPs with different dimensionalities, we utilize ultraviolet–visible (UV–vis) and ultrafast TA spectroscopy. Multiple absorption features of respective RDPs are disclosed in Figure S9 (Supporting Information). Interestingly, DJ RDPs ($n = 4$) show only small signals of lower-n phases, corroborating the minor presence of lower-n phases compared to the predominant 3D-like phase. **Figure 3A–D** shows TA contour plots as a function of pump-probe delay time. For RP RDPs, distinct ground state bleach peaks (GSBs) at $\approx$567, 607, 640, and 718 nm correspond to the $n = 2$, 3, 4, and 3D-like phases (GSB$_{n = \infty}$), whereas for DJ RDPs, the GSBs peaks of $n = 2$, 3, and 3D-like phases are located at $\approx$564, 609, and 746 nm, respectively. The temporal evolution of TA spectra shows GSBs features with high-energy tails near the band edge as well as the photo-induced absorption (PIA) signals.[35] As shown in Figure 3E,F, RP RDPs ($n = 2$) have a dominant GSB$_{n = 2}$ peak, whereas DJ RDPs ($n = 2$) have a broad phase distribution. In addition, in comparison to DJ RDPs ($n = 4$) which have a relatively uniform phase distribution, features with lower n phase in RP RDPs ($n = 4$) are enhanced (Figure 3G,H). We also notice a redshift of the 3D-like phase in both RP and DJ with higher dimensionality, which might be caused by hot carrier cooling or energy transfer from the "intermediate phase" to a

3D-like phase.[36,37] To quantitively evaluate the relative contents of each phase, we integrate the respective GSB peak at a time delay of 1 ps and normalize to the maximum value (Figure 3I, detailed analysis in Table S1, Supporting information). Notably, we find that the RP RDPs with lower dimensionality demonstrate a dominant $n = 2$ phase (85%) compared with DJ RDPs (40%), suggesting their phase purity. RDPs with higher dimensionality show an opposite trend, where DJ RDPs consist of a large population of larger-n phases ($n > 3$, 60%) compared to RP RDPs.

To compare the charge carrier behaviors in the respective RDPs, we take the TA kinetics of the representative GSBs (i.e., the GSB$_{n = 2}$ peak for RDPs with lower dimensionality and GSB$_{n = \infty}$ for RDPs with higher dimensionality) and plot them against delay time (Figure 3J,K). We find that the TA decay in the GSB$_{n = 2}$ region of DJ ($n = 2$) RDPs is faster than that of RP RDPs, whereas the decay of GSBs (3D-like phase) of RP ($n = 4$) RDPs is faster than that of DJ RDPs. The complex charge carrier dynamics between different phases can be only fitted qualitatively, i.e., without a firm physical model (detailed analysis in Table S2, Supporting information). In the case of GSBs$_{n = 2}$ of RDPs ($n = 2$), RP RDPs exhibit an average lifetime of 167.6 ps, which is higher than that of DJ RDPs (11.91 ps). The faster decay in DJ might relate to energy transfer from lower-n phases to higher-n phases, arising from the large population of isotropic lower-n phases.[38] Contrary to GSBs ($n = 2$), the average lifetime of GSBs$_{n = \infty}$ in DJ RDPs ($n = 4$) is 893.21 ps, which is two times higher than that of RP RDPs (391.86 ps) and likely related to their larger population of radiative recombination channels. In addition, the GSBs peaks of lower-n phases undergo fast decay accompanied by a rising signal of larger-n phases (Figure S11, Supporting information), indicating charge carrier transfer and accumulation in larger-n phases.[39–41]

In addition to examining the structure and charge carrier behaviors of RDPs with different dimensionalities, confocal-PL measurements (**Figure 4**) are utilized to map out the lifetime and film heterogeneity of respective RDPs. Prior to showing the confocal PL results, we also examine the surface morphology and roughness of the respective RDPs to rule out the effects of morphology defects (Figure S12, Supporting information). The root-mean-square roughness (RMS) of lower-dimensional RP RDPs (26.9 nm) is lower than that of DJ RDPs (31.9 nm). For RDPs with increasing dimensionality, RP ($n = 4$) exhibits an RMS of 12.3 nm compared to DJ (17.4 nm). Unlike RDPs ($n = 4$), those with lower dimensionality, particularly DJ RDPs, exhibit distinct film heterogeneity (Figure 4A,B). The dark regions in Figure 4B correspond to reduced average PL lifetime, indicating a higher concentration of defects serving as non-radiative recombination centers over micrometer length scales.[42] In contrast, we observe film homogeneity in RDPs ($n = 4$, Figure 4D,E). In addition, we extract the average radiative lifetime of respective RDPs (Figure 4C,F), where RP RDPs ($n = 2$) exhibit a longer average radiative lifetime (10.6 ns) compared to DJ RDPs (3.0 ns), indicating a decrease in the nonradiative recombination loss of RP RDPs with lower dimensionality. Interestingly, when increasing the dimensionality, we observe a different trend, that is, DJ RDPs ($n = 4$) reveal a longer average radiative lifetime of 37.6 ns, which is four times higher than that of RP RDPs. This indicates that DJ RDPs ($n = 4$) exhibit a reduced non-radiative recombination

ADVANCED
SCIENCE NEWS

www.advancedsciencenews.com

ADVANCED
FUNCTIONAL
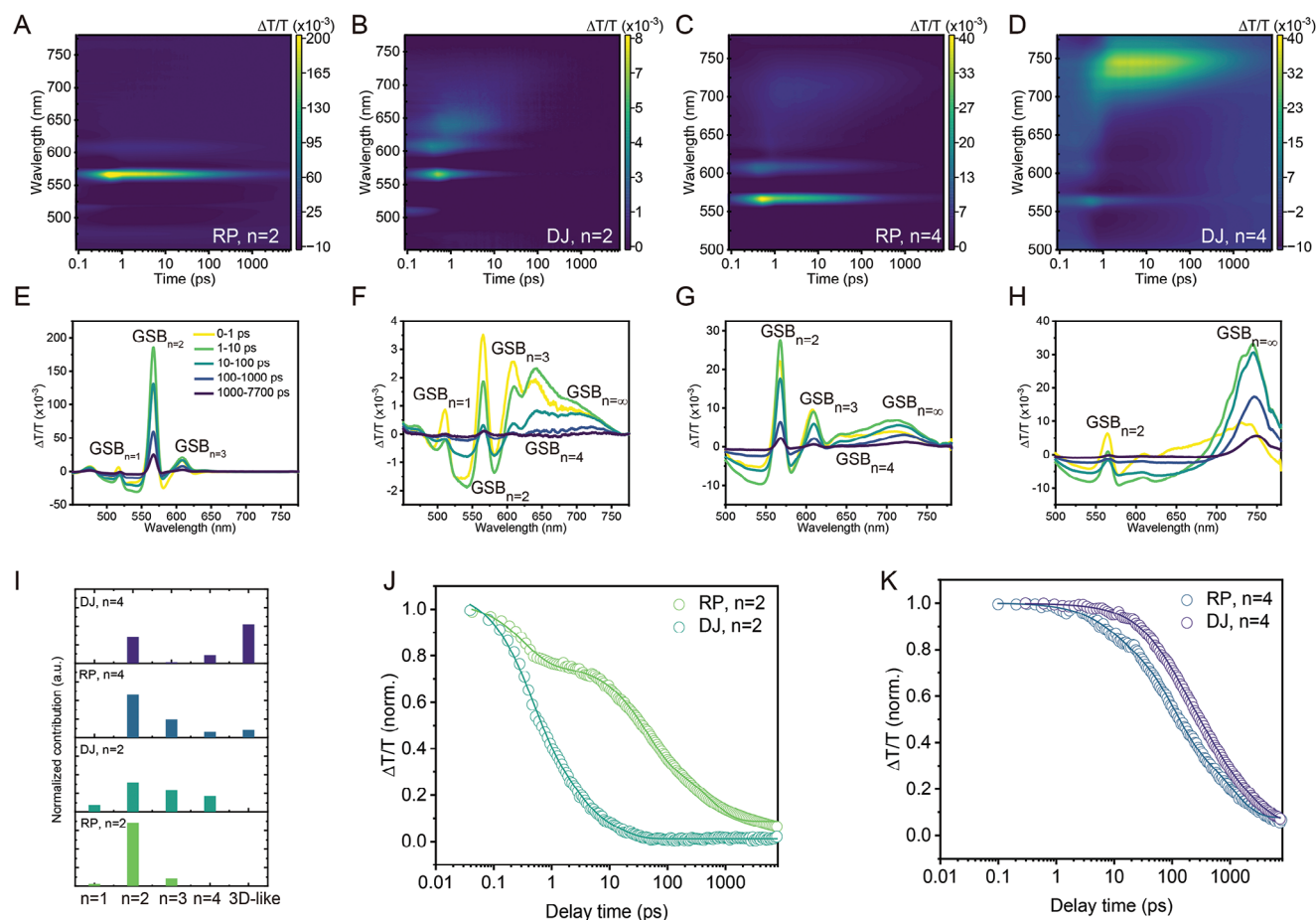**MATERIALS**

www.afm-journal.de

Figure 3. Charge carrier behavior of RDPs. Transient absorption maps of A) RP RDPs ($n = 2$), B) DJ RDPs ($n = 2$), C) RP RDPs ($n = 4$), and D) DJ RDPs ($n = 4$), where the RDPs were deposited on glass substrates. TA spectra at selected time delays after excitation of E) RP RDPs ($n = 2$), F) DJ RDPs ($n = 2$), G) RP RDPs ($n = 4$), and H) DJ RDPs ($n = 4$). TA spectra were collected following photoexcitation at 430 nm with pump fluence of ≈200 µJ cm^{-2}. I) Relative contribution from different phases of respective RDPs to the TA signal, as calculated from the amplitudes of the respective GSBs in TA spectra at 1 ps. Recombination dynamics at J) $GSB_{n=2}$ of RDPs ($n = 2$) and K) $GSB_{n=\infty}$ of RDPs ($n = 4$).

compared with RP RDPs. It should be noted that due to differences in detected spectral ranges, applied excitation fluences, and local diffusion effects,[43] direct comparison of charge carrier lifetimes obtained from confocal PL and TA spectra measurements is less feasible.

Collectively, a systematical study of structural and photophysical properties of RDPs with representative dimensionalities ($n = 2$, 4) would contribute significantly to the utilization of RDPs in solar cell applications. RP RDPs with lower dimensionality exhibit a dominant $n = 2$ phase, vertical orientation, longer charge carrier lifetime, and homogeneity, as confirmed by GIWAXS and TA. These characteristics could potentially make them more suitable as passivation layers in 2D/3D PSCs. Conversely, DJ RDPs with higher dimensionality demonstrate phase purity, a higher contribution of oriented crystals, spatially vertical phase homogeneity, and longer charge carrier lifetimes, rendering them more suitable for PSCs compared to RP RDPs. In addition, based on the optoelectronic properties of RP and DJ RDPs with higher dimensionality along with the band structures retrieved from the literature,[4,36,37] we propose an energy level diagram (Figure S13, Supporting information).

We observe an energy alignment mismatch between the $n<3$ phase and hole transport layer (HTL), resulting in inefficient hole extraction. Therefore, reducing the contribution of the lower-n phase can facilitate the hole transport in inverted quasi-2D PSCs.

We further use PL to investigate the intrinsic stability of RDPs ($n = 4$) under light illumination (**Figure 5A,B**). The peak corresponding to the 3D-like phase shows a redshift in both cases, along with brightening for the first 30 min, indicative of a decrease in trap density.[44] After illuminating for 60 min, we observe a blueshift in RP RDPs from 752.2 to 749.7 nm (Figure 5C) and a slight blueshift in DJ RDPs from 771.2 to 770.3 nm, suggesting that the population fraction of "intermediate phase" is increasing. To evaluate the device stability under light illumination, we monitor devices under the protocol of ISOS-L-1l and concurrently track the phase evolution of RDPs with operando GIWAXS.[45] The devices are fabricated with an inverted architecture of ITO/PEDOT:PSS/RDPs/PC61BM/BCP/Ag. The champion device performance of RP and DJ are shown in Figure S14A (Supporting Information), in which the champion device of RP exhibits a power conversion efficiency (*PCE*) of 8.84%, a

ADVANCED
SCIENCE NEWS

www.advancedsciencenews.com

ADVANCED
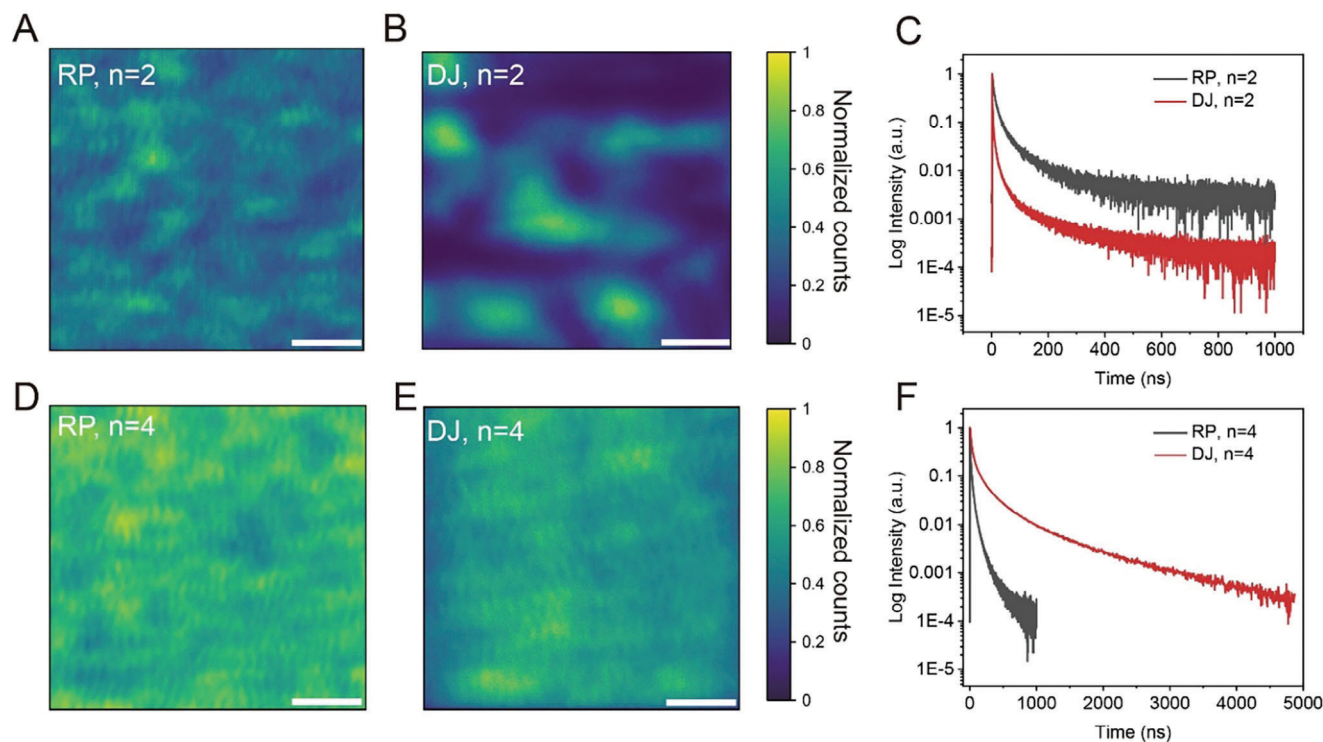FUNCTIONAL
MATERIALS

www.afm-journal.de

Figure 4. Film homogeneity and average radiative lifetime of RDPs. Confocal PL maps of encapsulated perovskite films with a 404 nm excitation (10 MHz; 0.1 µJ cm^{-2} per pulse), with scale bars (2 µm). A) RP RDPs ($n = 2$), B) DJ RDPs ($n = 2$), D) RP RDPs ($n = 4$), and E) DJ RDPs ($n = 4$). Statistics of average photoluminescence lifetime of (E) RDPs ($n = 2$) and F) RDPs ($n = 4$). Time-resolved PL measurements of (C) RDPs ($n = 2$) and F) RDPs ($n = 4$) using a 404 nm excitation.

short-circuit current (J_{SC}) of 13.67 mA cm^{-2}, an open-circuit voltage (V_{OC}) of 0.92 V, and a fill factor (FF) of 70.02%. The DJ-based device displays a PCE of 11.16%, a J_{SC} of 14.73 mA cm^{-2}, a V_{OC} of 1.04 V, and a FF of 72.42%. We notice that DJ-based devices exhibit excellent reproducibility and narrow performance distributions (Figure S14B–E, Supporting information) in comparison to RP-based devices. Together with GWIAXS and TA data, we identify three main factors that lead to the variations in device performances, i.e., phase purity, crystal orientation, and energy transfer. On the one hand, the prevalence of lower-n phases in RP RDPs, particularly the isotropic ones, is detrimental to charge transport, resulting in charge recombination and the loss of short-current density.[46] On the other hand, the inhomogeneous energy landscape caused by the phase impurities leads to inefficient energy transfer from lower-n phases to 3D-like phases. The energy disorder, including band structure, charge transport, and phase distribution disorder, deteriorates the V_{OC}.[47,48] In addition, we speculate that the non-radiative recombination at the interface of the 3D-like phase and lower-n phase constrains the FF.

The solar cell performance as a function of time is mapped out in Figure 5E,G. After 150 min of continuous illumination, the DJ-based device shows negligible degradation (Figure S15, Supporting information), whereas the RP-based device remains at 89% of its initial PCE. Synchrotron-based operando GIWAXS as a function of time is shown in Figure S16 (Supporting Information). Figure 5F,H demonstrates that the peaks located at $q \approx 1.0$ Å^{-1} of RP and DJ-based devices decrease in inten-

sity and shift to a higher q value, manifesting a lattice compressive strain in all directions. To quantitatively analyze the GI-WAXS, we use a Gaussian profile to fit the peak of $q \approx 1.0$ Å^{-1} (Figure 5I). Interestingly, we notice an appreciable increase of strain in the first 40 min in the RP device, followed by a slower increase of strain for the next 60 min. This behavior is in line with the degradation of solar cell performance. Moreover, the strain can also affect the interfaces between different phases in RP, consequently resulting in the degradation of FF. Overall, the RP-based device displays a compressive strain of 0.62% after 150 min of continuous illumination, which is four times higher than that of the DJ-based device (0.13%). In particular, we observe a larger strain along the out-of-plane direction compared to the in-plane direction in the RP-based device (Figures S17 and S18, Supporting information). This strain variation in RP and DJ-based devices is correlated with the existence of interfaces induced by phase impurity and their atomic structural rigidity, where the adjacent PbI$_6$ octahedra of DJ RDPs is directly connected by the long ligand, resulting in a reduced thickness of I•••I distance (7.18 Å),[49] a lower structural distortion and thus enhanced structural rigidity compared to RP RDPs (∼8.47 Å).[50,51]

3. Conclusion

In summary, we unravel the structural-photophysical properties of slot-die-coated RP and DJ RDPs with modifying dimensionalities. GIWAXS data confirm that RP RDPs with lower
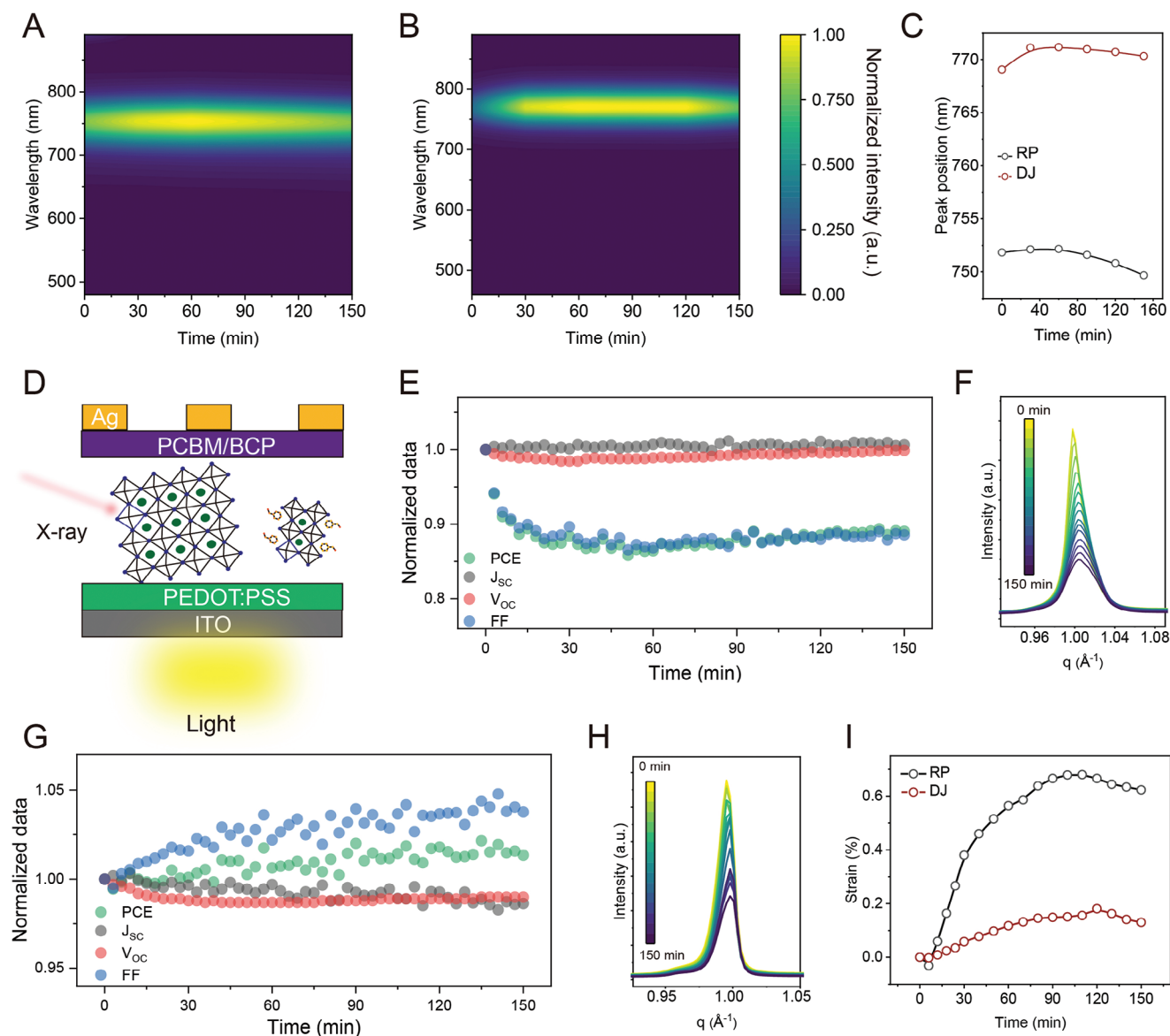
2411153 (7 of 11)

Figure 5. Stability of RDPs ($n = 4$) films and their device under continuous light illumination. The 2D contour plots of normalized photoluminescence as a function of time for A) RP RDPs, B) DJ RDPs, and C) peak positions of the 3D-like phase of RP and DJ RDPs versus time. D) A schematic illustration of devices operated under AM 1.5 G illumination with concomitant GIWAXS measurement. The solar cell performance as a function of time under the illumination of E) RP-based PSCs and G) DJ-based PSCs. F) Zoom-in pseudo-XRD acquired from 2D GIWAXS data of F) RP-based device and H) DJ-based device as a function of time. I) Evolution of strain derived from (F) and (H). The strain is defined by the q shift relative to the original q value, i.e., calculated by $(q_t-q_0)/q_0$, where t and q_0 represent the time of light illumination and the initial q value, respectively.

dimensionality exhibit a uniform phase distribution and preferential orientation along the out-of-plane direction, which favors charge transport in solar cells. In addition, they have a longer charge carrier lifetime and better film homogeneity in comparison to DJ RDPs, demonstrating the potential to form an ideal 2D/3D heterostructure with desired phase and orientation. In situ GIWAXS discloses the growth kinetics of respective RDPs, showing that the formation of lower-n phases is governed by stoichiometry and the formation energy. Thus, the formation of lower-n phases in RP RDPs is more favorable than in DJ RDPs. This highlights the potential of DJ RDPs in narrowing the phase distribution and thereafter a homogenous energy

landscape. When the dimensionality increases, DJ RDPs demonstrate highly concentrated phase distributions, pronounced orientation, spatially vertical phase homogeneity, and longer charge carrier lifetime, which enhances their device performance and stability under light illumination. Despite solvents and the film deposition method affecting the kinetics and leading to variations in structural properties, our work demonstrates that a rational design of the device architecture - by combining RP RDPs with lower dimensionality as the interface passivation layer and DJ RDPs as the active layer - can alleviate phase impurities and crystal random orientation, potentially achieving highly efficient and large-scale reduced-dimensional PSCs.

**ADVANCED
SCIENCE NEWS**

www.advancedsciencenews.com

**ADVANCED
FUNCTIONAL
MATERIALS**

www.afm-journal.de

4. Experimental Section

Materials: Lead iodide (PbI$_2$, 99%), phenethylammonium iodide (PEAI, 98%), methylammonium iodide (MAI, 99%), N,N-anhydrous dimethylformamide (DMF, 99.8%), dimethyl sulfoxide (DMSO, 99.9%), 2-propanol (IPA, 99.9%) [6,6]-phenyl C61 butyric acid methyl ester (PC61BM, 99.5%), and chlorobenzene (CB, 99.8%) were purchased from Sigma-Aldrich. 1,4-phenylenedimethanammonium (PDMAI$_2$, 99.5%) was purchased from Xi'an Polymer Light Technology Corporation. Poly(3,4-ethylenedioxythiophene) polystyrene sulfonate (PEDOT:PSS, BaytronP-VPAI4083) and bathocuproine (BCP, 99%) were purchased from Ossila and TCI, respectively. All materials were used as received without any other refinement unless otherwise specified.

Precursors Preparation and Film Deposition: The 2D RP ((PEA)$_2$MA$_{n-1}$Pb$_n$I$_{3n+1}$) perovskite and DJ (PDMA)MA$_{n-1}$Pb$_n$I$_{3n+1}$ perovskite solutions were prepared by dissolving the appropriate stoichiometric quantities of PbI$_2$, MAI, and PEAI or PDMAI$_2$ in a mixture of DMF and DMSO (9:1, v/v), where the concentration of Pb^{2+} is 0.5 M. The solutions were stirred at 70 °C until fully dissolved and cooled down to room temperature before use. The patterned ITO (75×25 mm) or glass substrates were rinsed in the sequence of diluted Hellmanex III (2:98), DI water, acetone, ethanol, and isopropanol in the ultrasonic bath for 15 min each. The substrates were treated with an O$_2$ plasma before further processing. Subsequently, the perovskite precursor was slot-die-coated on a preheated substrate (70 °C) with a coating speed of 5 mm s^{-1}. The pumping speed was 110 µL min^{-1}, and the gap height was 200 µm. The N$_2$ knife was set at a 45-degree angle against the printing direction with a pressure of 10 psi. Afterward, the samples were annealed at 100 °C for 10 min. Details about the slot-die coater can be found elsewhere.[52]

Device Fabrication: The inverted solar cells had a device structure of ITO/PEDOT:PSS/perovskite/PC61BM/BCP/Ag. The PEDOT:PSS was filtered and spin-coated on O$_2$-plasma treated ITO substrates at 4000 rpm for 30 s, and then annealed at 150 °C in air for 30 min. Afterward, the perovskite was deposited as described above. The PC61BM solution (20 mg mL^{-1} in CB) was dynamically spin-coated on ITO/PEDOT:PSS/perovskite layers at 3000 rpm for 30 s. Afterward, the BCP (0.5 mg mL^{-1} in IPA) solutions were dynamically deposited at 3000 rpm for 30 s. Finally, a 100 nm thick Ag was evaporated under a vacuum of 1 × 10^{-6} Pa.

Materials Characterization—GIWAXS: All GIWAXS data (in and ex situ) were collected at beamline P03 at PETRA III synchrotron (DESY, Hamburg).[53] In situ, 2D GIWAXS data was collected under an incidence angle of 0.4° with an X-ray beam energy of 11.8 keV and recorded on a LAMBDA 9 M detector (X-Spectrum). In the kinetic study of the film growth, the perovskite layer was slot-die coated on heated ITO substrates (70 °C), and the data was recorded with an exposure time of 0.2 s. Operando 2D GIWAXS data was collected under an incident angle of 0.6° with an X-ray beam energy of 11.83 keV, whereas an exposure time of 1 s was used. The operando GIWAXS measurement on the quasi-2D perovskite solar cells was done via the ISOS-L-1I protocol (i.e., under the continuous bias scan and light illumination).[45,54] In addition, the entire chamber was connected with cooling water (25 °C) to preclude the temperature-induced degradation.[55] Angular-dependent X-ray scattering data was collected with an X-ray beam energy of 12.92 keV with a sample-to-detector distance (SDD) of 279.25 mm. The scattering depth was calculated using https://gixa.ati.tuwien.ac.at/tools/penetrationdepth.xhl.[56] The positions of the beam center and SDD in all measurements were calibrated by fits to the patterns of LaB$_6$ and CeO$_2$ with the DPDAK package.[57] The reshaped 2D GIWAXS data, the line cuts, and the azimuthal integration of the scattering data were processed with the Python tool INSIGHT (20, 49). The correction of SDD was done by calibrating the ITO peak to $q = 2.132$ Å^{-1}. The GIWAXS data was indexed according to the literatures.[49,58] The I•••I distance was calculated based on the structures of RP and DJ in these literatures.[49,51]

Materials Characterization—Film characterization: The optical absorption spectra were measured with an ultraviolet/visible (UV/Vis) spectrophotometer (Perkin Elmer Lambda 35). Atomic Force Microscopy (AFM) measurements were carried out with an AFM instrument (Nanosurf, FlexAFM, Switzerland). The photoluminescence spectra were detected by a fluorescence spectrometer (PerkinElmer LS 55) with an excitation wavelength of 450 nm and a slit width of 15 nm. Photoluminescence mapping was performed using a confocal time-correlated single-photon counting (TCSPC) setup (PicoQuant, MicroTime 200). A 404 nm pulsed laser with an average power of 100 mW cm^{-2} (0.1 µJ cm^{-2} per pulse), operating at repetition rates of 10 MHz for various perovskite films, was focused onto the sample using a ×100 objective. The resulting data were smoothed by averaging nearby data points spatially and temporally. PL was collected across a region of 10 µm × 10 µm.[59] The average radiative lifetime was used as a means to mathematically quantify the lifetime and statistically compare the decay times between samples, but it was stressed that any physical model on this was not invoking.

Materials Characterization—Transient Absorption Characterization: Commercial TA spectrometers (Ultrafast Systems, HELIOS, and EOS) were used. The relative content of the respective phase in RDPs can be quantified by the amplitude of the GSBs peak signal as:[60]

$$p_{ni} = \frac{\int_{n_i} \Delta A \, dE}{\int_n \Delta A \, dE} \tag{1}$$

where p_{ni} and ΔA is the relative content of the respective phase and the amplitude of the GSBs signal of each phase, respectively. All TA data were collected for photoexcitation at 430 nm with a pump fluence of ≈200 µJ cm^{-2}.

Materials Characterization—Solar cell characterization: The current density–voltage (J–V) measurement was conducted with a Keithley 2611B source meter under the light illumination of the solar simulator (class ABA, Newport) at a light intensity of 100 mW cm^{-2}, where the light intensity was calibrated by a reference solar cell (Fraunhofer ISE019-2015). The solar cells were measured with a scan rate of 50 mV S^{-1} (voltage steps of 10 meV and a delay time of 100 ms). The solar cell devices were measured by masking the active area with a metal mask of 0.079 cm^2.

Supporting Information

Supporting Information is available from the Wiley Online Library or from the author.

Conflict of Interest

The authors declare no conflict of interest.

Data Availability Statement

The data that support the findings of this study are available from the corresponding author upon reasonable request.

**ADVANCED
SCIENCE NEWS**

www.advancedsciencenews.com

**ADVANCED
FUNCTIONAL
MATERIALS**

www.afm-journal.de

[1] J.-C. Blancon, J. Even, C. C. Stoumpos, M. G. Kanatzidis, A. D. Mohite, *Nat. Nanotechnol.* **2020**, *15*, 969.

[2] G. Grancini, M. K. Nazeeruddin, *Nat. Rev. Mater.* **2019**, *4*, 4.

[3] T. He, S. Li, Y. Jiang, C. Qin, M. Cui, L. Qiao, H. Xu, J. Yang, R. Long, H. Wang, *Nat. Commun.* **2020**, *11*, 1672.

[4] S. Sidhik, Y. Wang, M. De Siena, R. Asadpour, A. J. Torma, T. Terlier, K. Ho, W. Li, A. B. Puthirath, X. Shuai, *Science* **2022**, *377*, 1425.

[5] K. Ma, J. Sun, H. R. Atapattu, B. W. Larson, H. Yang, D. Sun, K. Chen, K. Wang, Y. Lee, Y. Tang, *Sci. Adv.* **2023**, *9*, eadg0032.

[6] F. Zhang, S. Y. Park, C. Yao, H. Lu, S. P. Dunfield, C. Xiao, S. Uličná, X. Zhao, L. Du Hill, X. Chen, *Science* **2022**, *375*, 71.

[7] Y. Shang, Y. Liao, Q. Wei, Z. Wang, B. Xiang, Y. Ke, W. Liu, Z. Ning, *Sci. Adv.* **2019**, *5*, eaaw8072.

[8] B. R. Sutherland, E. H. Sargent, *Nat. Photonics* **2016**, *10*, 295.

[9] H. Gu, J. Xia, C. Liang, Y. Chen, W. Huang, G. Xing, *Nat. Rev. Mater.* **2023**, *8*, 533.

[10] P. Cheng, P. Wang, Z. Xu, X. Jia, Q. Wei, N. Yuan, J. Ding, R. Li, G. Zhao, Y. Cheng, *ACS Energy Lett.* **2019**, *4*, 1830.

[11] C. Liang, H. Gu, Y. Xia, Z. Wang, X. Liu, J. Xia, S. Zuo, Y. Hu, X. Gao, W. Hui, *Nat. Energy* **2021**, *6*, 38.

[12] M. Worku, Q. He, L.-J. Xu, J. Hong, R. X. Yang, L. Z. Tan, B. Ma, *ACS Appl. Mater. Interfaces* **2020**, *12*, 45056.

[13] J. Qing, X. K. Liu, M. Li, F. Liu, Z. Yuan, E. Tiukalova, Z. Yan, M. Duchamp, S. Chen, Y. Wang, *Adv. Energy Mater.* **2018**, *8*, 1800185.

[14] J. Zhang, J. Qin, M. Wang, Y. Bai, H. Zou, J. K. Keum, R. Tao, H. Xu, H. Yu, S. Haacke, *Joule* **2019**, *3*, 3061.

[15] D. B. Kim, S. Lee, C. H. Jang, J. H. Park, A. Lee, M. H. Song, *Adv. Mater. Interfaces* **2020**, *7*, 1902158.

[16] M. Xiong, M. Zou, K. Fan, C. Qin, S. Li, L. Fei, J. Jiang, H. Huang, L. Shen, F. Gao, *ACS Energy Lett.* **2022**, *7*, 550.

[17] R. Azmi, E. Ugur, A. Seitkhan, F. Aljamaan, A. S. Subbiah, J. Liu, G. T. Harrison, M. I. Nugraha, M. K. Eswaran, M. Babics, *Science* **2022**, *376*, 73.

[18] E. Shi, B. Yuan, S. B. Shiring, Y. Gao, Akriti, Y. G., C. Su, M. Lai, P. Yang, J. Kong, *Nature* **2020**, *580*, 614.

[19] Y. Gao, E. Shi, S. Deng, S. B. Shiring, J. M. Snaider, C. Liang, B. Yuan, R. Song, S. M. Janke, A. Liebman-Peláez, *Nat. Chem.* **2019**, *11*, 1151.

[20] H. Chen, S. Teale, B. Chen, Y. Hou, L. Grater, T. Zhu, K. Bertens, S. M. Park, H. R. Atapattu, Y. Gao, M. Wei, A. K. Johnston, Q. Zhou, K. Xu, D. Yu, C. Han, T. Cui, E. H. Jung, C. Zhou, W. Zhou, A. H. Proppe, S. Hoogland, F. Laquai, T. Filleter, K. R. Graham, Z. Ning, E. H. Sargent, *Nat. Photonics* **2022**, *16*, 352.

[21] J. M. Hoffman, J. Strzalka, N. C. Flanders, I. Hadar, S. A. Cuthriell, Q. Zhang, R. D. Schaller, W. R. Dichtel, L. X. Chen, M. G. Kanatzidis, *Adv. Mater.* **2020**, *32*, 2002812.

[22] J. M. Hoffman, I. Hadar, X. Li, W. Ke, E. S. Vasileiadou, J. Strzalka, L. X. Chen, M. G. Kanatzidis, *Chem* **2022**, *8*, 1067.

[23] J.-C. Blancon, A. V. Stier, H. Tsai, W. Nie, C. C. Stoumpos, B. Traore, L. Pedesseau, M. Kepenekian, F. Katsutani, G. Noe, *Nat. Commun.* **2018**, *9*, 2254.

[24] D. Ghosh, D. Acharya, L. Pedesseau, C. Katan, J. Even, S. Tretiak, A. J. Neukirch, *J. Mater. Chem. A* **2020**, *8*, 22009.

[25] J. Zhang, J. Qin, M. Wang, Y. Bai, H. Zou, J. K. Keum, R. Tao, H. Xu, H. Yu, S. Haacke, B. Hu, *Joule* **2019**, *3*, 3061.

[26] Y. Li, J. V. Milić, A. Ummadisingu, J.-Y. Seo, J.-H. Im, H.-S. Kim, Y. Liu, M. I. Dar, S. M. Zakeeruddin, P. Wang, A. Hagfeldt, M. Grätzel, *Nano Lett.* **2019**, *19*, 150.

[27] L. N. Quan, Y. Zhao, F. P. García de Arquer, R. Sabatini, G. Walters, O. Voznyy, R. Comin, Y. Li, J. Z. Fan, H. Tan, *Nano Lett.* **2017**, *17*, 3701.

[28] M. A. Reus, L. K. Reb, A. F. Weinzierl, C. L. Weindl, R. Guo, T. Xiao, M. Schwartzkopf, A. Chumakov, S. V. Roth, P. Müller-Buschbaum, *Adv. Opt. Mater.* **2022**, *10*, 2102722.

[29] W. L. Tan, N. M. Kirby, Y.-B. Cheng, C. R. McNeill, *Nano Energy* **2021**, *83*, 105818.

[30] L. N. Quan, M. Yuan, R. Comin, O. Voznyy, E. M. Beauregard, S. Hoogland, A. Buin, A. R. Kirmani, K. Zhao, A. Amassian, *J. Am. Chem. Soc.* **2016**, *138*, 2649.

[31] P. Fu, S. Liu, S. Yu, H. Yin, B. Yang, S. Ahmad, X. Guo, C. Li, *Nano Energy* **2021**, *88*, 106249.

[32] J. Qiu, Y. Zheng, Y. Xia, L. Chao, Y. Chen, W. Huang, *Adv. Funct. Mater.* **2019**, *29*, 1806831.

[33] H. Chen, S. Teale, B. Chen, Y. Hou, L. Grater, T. Zhu, K. Bertens, S. M. Park, H. R. Atapattu, Y. Gao, *Nat. Photonics* **2022**, *16*, 352.

[34] R. Quintero-Bermudez, A. Gold-Parker, A. H. Proppe, R. Munir, Z. Yang, S. O. Kelley, A. Amassian, M. F. Toney, E. H. Sargent, *Nat. Mater.* **2018**, *17*, 900.

[35] M. B. Price, J. Butkus, T. C. Jellicoe, A. Sadhanala, A. Briane, J. E. Halpert, K. Broch, J. M. Hodgkiss, R. H. Friend, F. Deschler, *Nat. Commun.* **2015**, *6*, 8420.

[36] Y. Lin, Y. Fang, J. Zhao, Y. Shao, S. J. Stuard, M. M. Nahid, H. Ade, Q. Wang, J. E. Shield, N. Zhou, *Nat. Commun.* **2019**, *10*, 1008.

[37] Q. Shang, Y. Wang, Y. Zhong, Y. Mi, L. Qin, Y. Zhao, X. Qiu, X. Liu, Q. Zhang, *J. Phys. Chem. Lett.* **2017**, *8*, 4431.

[38] A. Stadlbauer, L. Eyre, A. Biewald, F. Rauh, M. W. Heindl, S. Liu, J. Zerhoch, S. Feldmann, A. Hartschuh, F. Deschler, *Adv. Opt. Mater.* **2023**, *12*, 2301331.

[39] Y. Jiang, C. Qin, M. Cui, T. He, K. Liu, Y. Huang, M. Luo, L. Zhang, H. Xu, S. Li, *Nat. Commun.* **2019**, *10*, 1868.

[40] G. Xing, B. Wu, X. Wu, M. Li, B. Du, Q. Wei, J. Guo, E. K. Yeow, T. C. Sum, W. Huang, *Nat. Commun.* **2017**, *8*, 14558.

[41] C. Qin, L. Xu, Z. Zhou, J. Song, S. Ma, Z. Jiao, Y. Jiang, *J. Mater. Chem. A* **2022**, *10*, 3069.

[42] Y. Sun, L. Ge, L. Dai, C. Cho, J. Ferrer Orri, K. Ji, S. J. Zelewski, Y. Liu, A. J. Mirabelli, Y. Zhang, *Nature* **2023**, *615*, 830.

[43] E. M. Tennyson, T. A. Doherty, S. D. Stranks, *Nat. Rev. Mater.* **2019**, *4*, 573.

[44] R. E. Beal, N. Z. Hagström, J. Barrier, A. Gold-Parker, R. Prasanna, K. A. Bush, D. Passarello, L. T. Schelhas, K. Brüning, C. J. Tassone, H.-G. Steinrück, M. D. McGehee, M. F. Toney, A. F. Nogueira, *Matter* **2020**, *2*, 207.

[45] M. V. Khenkin, E. A. Katz, A. Abate, G. Bardizza, J. J. Berry, C. Brabec, F. Brunetti, V. Bulović, Q. Burlingame, A. Di Carlo, R. Cheacharoen, Y.-B. Cheng, A. Colsmann, S. Cros, K. Domanski, M. Dusza, C. J. Fell, S. R. Forrest, Y. Galagan, D. Di Girolamo, M. Grätzel, A. Hagfeldt, E. von Hauff, H. Hoppe, J. Kettle, H. Köbler, M. S. Leite, S. Liu, Y.-L. Loo, J. M. Luther, et al., *Nat. Energy* **2020**, *5*, 35.

[46] Y. Lin, Y. Fang, J. Zhao, Y. Shao, S. J. Stuard, M. M. Nahid, H. Ade, Q. Wang, J. E. Shield, N. Zhou, A. M. Moran, J. Huang, *Nat. Commun.* **2019**, *10*, 1008.

[47] T. He, S. Li, Y. Jiang, C. Qin, M. Cui, L. Qiao, H. Xu, J. Yang, R. Long, H. Wang, M. Yuan, *Nat. Commun.* **2020**, *11*, 1672.

[48] J. Xu, O. Voznyy, M. Liu, A. R. Kirmani, G. Walters, R. Munir, M. Abdelsamie, A. H. Proppe, A. Sarkar, F. P. García de Arquer, M. Wei, B. Sun, M. Liu, O. Ouellette, R. Quintero-Bermudez, J. Li, J. Fan, L. Quan, P. Todorovic, H. Tan, S. Hoogland, S. O. Kelley, M. Stefik, A. Amassian, E. H. Sargent, *Nat. Nanotechnol.* **2018**, *13*, 456.

2411153 (10 of 11)

[49] Y. Liu, H. Zhou, Y. Ni, J. Guo, R. Lu, C. Li, X. Guo, *Joule* **2023**, *7*, 1016.

[50] W. Li, S. Sidhik, B. Traore, R. Asadpour, J. Hou, H. Zhang, A. Fehr, J. Essman, Y. Wang, J. M. Hoffman, I. Spanopoulos, J. J. Crochet, E. Tsai, J. Strzalka, C. Katan, M. A. Alam, M. G. Kanatzidis, J. Even, J.-C. Blancon, A. D. Mohite, *Nat. Nanotechnol.* **2022**, *17*, 45.

[51] M. A. K. Sheikh, D. Kowal, M. H. Mahyuddin, R. Cala', E. Auffray, M. E. Witkowski, M. Makowski, W. Drozdowski, H. Wang, C. Dujardin, D. Cortecchia, M. D. Birowosuto, *J. Phys. Chem. C* **2023**, *127*, 10737.

[52] M. A. Reus, T. Baier, C. G. Lindenmeir, A. F. Weinzierl, A. Buyan-Arivjikh, S. A. Wegener, D. P. Kosbahn, L. K. Reb, J. Rubeck, M. Schwartzkopf, S. V. Roth, P. Müller-Buschbaum, *Rev. Sci. Instrum.* **2024**, *95*, 043907.

[53] A. Buffet, A. Rothkirch, R. Döhrmann, V. Körstgens, M. M. Abul Kashem, J. Perlich, G. Herzog, M. Schwartzkopf, R. Gehrke, P. Müller-Buschbaum, S. V. Roth, *J. Synchr. Radiat.* **2012**, *19*, 647.

[54] R. Guo, D. Han, W. Chen, L. Dai, K. Ji, Q. Xiong, S. Li, L. K. Reb, M. A. Scheel, S. Pratap, N. Li, S. Yin, T. Xiao, S. Liang, A. L. Oechsle, C. L. Weindl, M. Schwartzkopf, H. Ebert, P. Gao, K. Wang, M. Yuan, N. C. Greenham, S. D. Stranks, S. V. Roth, R. H. Friend, P. Müller-Buschbaum, *Nat. Energy* **2021**, *6*, 977.

[55] K. Sun, R. Guo, Y. Liang, J. E. Heger, S. Liu, S. Yin, M. A. Reus, L. V. Spanier, F. Deschler, S. Bernstorff, P. Müller-Buschbaum, *ACS Appl. Mater. Interfaces* **2023**, *15*, 30342.

[56] D. Ingerle, F. Meirer, G. Pepponi, E. Demenev, D. Giubertoni, P. Wobrauschek, C. Streli, *Spectrochim. Acta Part B: At. Spectrosc.* **2014**, *99*, 121.

[57] G. Benecke, W. Wagermaier, C. Li, M. Schwartzkopf, G. Flucke, R. Hoerth, I. Zizak, M. Burghammer, E. Metwalli, P. Muller-Buschbaum, M. Trebbin, S. Forster, O. Paris, S. V. Roth, P. Fratzl, *J. Appl. Crystallogr.* **2014**, *47*, 1797.

[58] W. Peng, J. Yin, K.-T. Ho, O. Ouellette, M. De Bastiani, B. Murali, O. El Tall, C. Shen, X. Miao, J. Pan, E. Alarousu, J.-H. He, B. S. Ooi, O. F. Mohammed, E. Sargent, O. M. Bakr, *Nano Lett.* **2017**, *17*, 4759.

[59] C. Cho, S. Feldmann, K. M. Yeom, Y.-W. Jang, S. Kahmann, J.-Y. Huang, T. C. J. Yang, M. N. T. Khayyat, Y.-R. Wu, M. Choi, J. H. Noh, S. D. Stranks, N. C. Greenham, *Nat. Mater.* **2022**, *21*, 1388.

[60] L. N. Quan, Y. Zhao, F. P. García de Arquer, R. Sabatini, G. Walters, O. Voznyy, R. Comin, Y. Li, J. Z. Fan, H. Tan, J. Pan, M. Yuan, O. M. Bakr, Z. Lu, D. H. Kim, E. H. Sargent, *Nano Lett.* **2017**, *17*, 3701.

2411153 (11 of 11)